Precision Engineering 62 (2020) 213–222

Contents lists available at ScienceDirect

Precision Engineering

journal homepage: http://www.elsevier.com/locate/precision

Effects of deep subsurface damages on surface nanostructure formation in laser recovery of grinded single-crystal silicon wafers

Keiichiro Niitsu [a], Jiwang Yan [b,*]

[a] School of Integrated Design Engineering, Graduate School of Science and Technology, Keio University, Hiyoshi 3-14-1, Kohoku-ku, Yokohama, 223-8522, Japan
[b] Department of Mechanical Engineering, Faculty of Science and Technology, Keio University, Hiyoshi 3-14-1, Kohoku-ku, Yokohama, 223-8522, Japan

ARTICLE INFO

Keywords:
single-crystal silicon
Laser recovery
Nanodot structure
Subsurface damage
Latent defect

ABSTRACT

A nanosecond pulsed Nd:YVO_4 laser was irradiated on a boron-doped single-crystal silicon wafer after rough and fine grinding processes to recover the grinding-induced subsurface damages. The surface topography of samples was investigated by using a white-light interferometer, a scanning electron microscope, and an atomic force microscope; while the crystallinity was analyzed by a laser micro-Raman spectrometer. It was found that surface nanostructures were generated by the Mullins-Sekerka instability, which remained on the surface under recoil pressure and surface tension. The rough grinding-induced deep subsurface damages influenced the interface instability between liquid and solid silicon during recrystallization process. By increasing pulse width and decreasing laser peak irradiance, the subsurface damage was recovered and a flat surface with surface roughness of ~1 nm Sa was obtained. This study reveals important correlations among grinding-induced latent subsurface defects, laser peak irradiance and nanoscale surface topography formation in laser recovery, which contributes to high quality silicon wafer manufacturing.

1. Introduction

Single-crystal silicon is an indispensable material in the semiconductor industry. Silicon wafers are produced from a single-crystal silicon ingot through a series of processes such as slicing, flatting, etching, grinding, and polishing [1]. These mechanical processes induced subsurface damages, which include amorphous layers, dislocations, and microcracks [2–7]. To eliminate the subsurface damages, chemo-mechanical polishing (CMP) is generally performed after fine grinding. However, in the wafer manufacturing process, CMP is a time-consuming bottleneck and has poor controllability. In order to solve this problem, innovative approaches are being explored.

In our previous research, a nanosecond pulsed laser irradiation was proposed to recover the subsurface damages which were generated by ultraprecision diamond cutting and fine grinding of single-crystal silicon wafers [8–12]. This process, called laser recovery, involves selectively melting and recrystallizing of the subsurface damaged material. A single-crystal structure is recreated due to epitaxial growth from the undamaged bulk. Furthermore, laser recovery technology can reduce the surface roughness by flatting grinding marks due to surface tension effect during melting. The laser recovery process is clean without pollution and waste emission. It will not cause material loss. Furthermore, the laser recovery process is fast. It is expected that by using a high power laser with a line beam scanning system, a 300 mm-diameter silicon wafer can be processed within a few minutes, which is faster than the conventional CMP processes. Though laser recovery is anticipated to be a new surface processing method, the recovery characteristics of deep subsurface damages caused by rough grinding, which is normally performed before fine grinding, is still unclear.

On the other hand, in order to apply laser recovery to silicon wafer fabrication, nanoscale surface smoothness is required. However, it has been reported that nanostructures will be generated on silicon materials by femtosecond laser [13–22], picosecond laser [23–27], and nanosecond laser [28–33]. A well-known phenomenon is the formation of laser-induced periodic surface structure (LIPSS). In general, there are two types of LIPSS according to the periods of ripples. Low spatial frequency LIPSS (LSFL) whose period closes to the laser wavelength is generated by surface plasomon polaritons (SPPs) [17–19]; high spatial frequency LIPSS (HSFL) has a smaller period than a half of laser wavelength. The formation mechanism of HSFL have been proposed such as self-organization [21,22] and second harmonic generation [16], etc., although the HSFL generation mechanism is still under investigation.

* Corresponding author.
E-mail address: yan@mech.keio.ac.jp (J. Yan).

https://doi.org/10.1016/j.precisioneng.2019.12.005
Received 3 December 2019; Accepted 9 December 2019
Available online 10 December 2019

Nanosecond laser also induced nanostructures such as LIPSS by SPPs [32], and dot structures [28–31]. The formation of such nanodot structures on a Si surface was *in situ* confirmed by using a pulsed-laser-equipped high-voltage electron microscope [31]. However, all the previous researches on laser-induced nanostructures of silicon have been performed by using pristine silicon wafers with chemo-mechanically polished surface, or thin film silicon; whereas the nanostructure formation on a grinded, especially rough-grinded, wafer with subsurface damage has not been studied yet.

The purpose of this study is to clarify the mechanism of surface nanostructure generation on a grinding-damaged silicon wafer with nanosecond pulsed laser irradiation. In particular, the effect of rough grinding-induced latent subsurface damages on interference instability between the liquid and solid silicon during recrystallization process will be investigated. This study will contribute to controlling and optimizing nanometer scale surface integrity of single-crystal silicon wafers in laser processing.

2. Process mechanisms

2.1. Laser recovery mechanism

Fig. 1 shows a schematic diagram of laser recovery mechanism of grinding-induced subsurface damages in a single-crystal silicon wafer. In general, rough grinding induces deep microcracks and stacking faults, whereas fine grinding causes subsurface damages such as amorphous silicon layers, dislocations, and shallow microcracks (Fig. 1(a)). Sometimes, the deep latent damages caused by rough grinding cannot be completely removed even after the subsequent fine grinding and thus remain in the wafer. During pulsed laser irradiation, a melted layer expands from top to bottom (Fig. 1(b)). When the melted layer is not deep enough, the rough grinding-induced subsurface damages will remain and affect the solid/liquid interface during resolidification. As a result, epitaxial growth becomes unstable. On the other hand, when the melted layer is deeper than the latent subsurface damages, the solid/liquid interface will reach the defect-free bulk. Therefore, stable epitaxial growth begins and a damage-free single-crystal structure is obtained.

2.2. Surface nanostructure formation mechanism

In the step of Fig. 1(b), due to the temperature profile of solid/liquid interface, protrusions will grow with Mullins-Sekerka instability, as schematically shown in Fig. 2. Liquid silicon near the interface is in a supercooling state [34]. Fig. 2(b) shows liquid/solid interface of silicon and isotherms of temperature. A part of the interface is slightly protuberated due to fluctuations, as shown in Fig. 2(c). The protrusion compresses the isotherms locally from flat interface. This local large temperature gradient makes an easy latent heat flow away from the interface. As a result, the growth of the protrusion is promoted drastically in comparison with the growth of flat interface. While the protrusion becomes more pronounced, surface tension due to the Gibbs-Thomson effect makes the protrusion a round shape as shown in Fig. 2(d). This instability on the interface is known as the Mullins-Sekerka instability [35]. The protrusion appears on the top surface as nanostructures through the repetitive growth and rounding process.

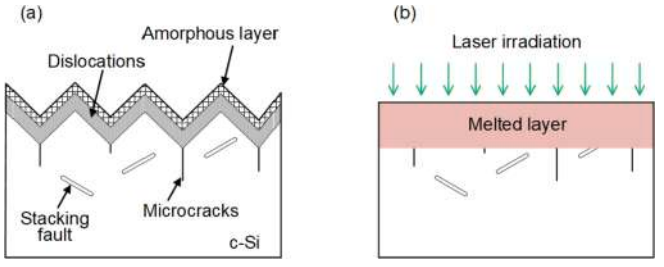

Fig. 1. Schematic diagram of laser recovery mechanism of grinding-induced surbsurface damages in a single-crystal silicon wafer.

2.3. Laser fluence and peak irradiance

The temperature profile at liquid-solid interface and subsequent nanostructure formation are dependent on laser fluence and peak irradiance. Fig. 3 shows a Gaussian pulse train of laser irradiation. Pulse energy E is calculated by the following equation:

$$E = \frac{P_{\text{ave}}}{f} \tag{1}$$

where P_{ave} is the average laser power and f is the repetition frequency. Then, laser fluence F with respect to radius of beam spot b is

$$F = \frac{E}{\pi b^2} \tag{2}$$

The laser fluence includes pulse width effect. Thus, in order to separate pulse width effect, laser peak irradiance is calculated in this study. $P(t)$ is assumed pulse profile, then pulse energy E is calculated by the following equation:

$$\begin{aligned} E &= \int_{-\infty}^{\infty} P(t)dt = \int_{-\infty}^{\infty} P_0 \exp\left(-\frac{(t-t_0)^2}{2\sigma^2}\right)dt \\ &= P_0 \int_{-\infty}^{\infty} \exp\left(-\frac{(t-t_0)^2}{2\sigma^2}\right)dt = P_0\sigma\sqrt{2\pi} \end{aligned} \tag{3}$$

where P_0 is peak power, t is time, t_0 is mean, and σ is standard deviation. Standard deviation σ is defined by:

$$\sigma = \frac{\tau}{2\sqrt{2\ln 2}} \tag{4}$$

where τ is pulse width.

As shown in Fig. 4, in case of the laser having a Gaussian distribution, irradiance $I(r)$ is defined by:

$$I(r) = I_0 \exp\left(-2\frac{r^2}{b^2}\right) \tag{5}$$

where I_0 is peak irradiance, and r is distance from the laser beam center. Peak power P_0 is calculated by volume integration of $I(r)$:

$$P_0 = \int_0^b I(r)2\pi r dr = \int_0^b I_0 \exp\left(-2\frac{r^2}{b^2}\right)2\pi r dr = \frac{\pi I_0 b^2}{2} \tag{6}$$

Thus, peak irradiance I_0 is defined by:

$$I_0 = \frac{2}{\pi b^2}P_0 = \frac{2}{\pi b^2}\frac{E}{\sigma\sqrt{2\pi}} \tag{7}$$

3. Experimental procedures

Boron-doped P++ single-crystal silicon wafers whose resistivity was 0.004–0.007 Ω·cm were used as specimen. The silicon wafers were prepared by two grinding processes using cup-shape grinding wheels: rough grinding with coarse diamond abrasive grains (grain size 5–10 μm) and fine grinding with diamond abrasive grains whose grain size was ~2 μm.

The laser used in the experiments was a Nd:YVO_4 laser Super Pulse 532–30 (Suzhou Inngu Laser Co., LTD, China), which had a wavelength of 532 nm. Laser irradiation was performed with a galvanometer mirror system in air. The beam diameter was 85 μm with a Gaussian distribution of energy density. The polarization of the beam was circular by using a quarter-wave plate to isolate returned laser. Pulse widths of 16,

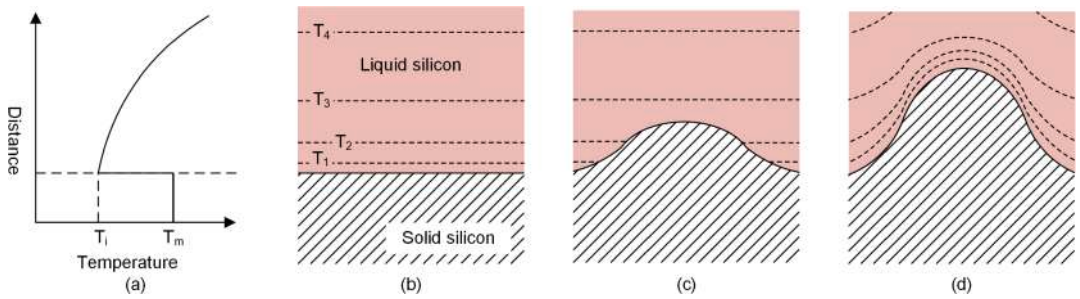

Fig. 2. (a) Temperature profile of solid/liquid interface, where T_m is melting point of single-crystal silicon. (b–d) Schematic diagrams of protrusion growing with Mullins-Sekerka instability, where the dashed lines are isotherms of temperature ($T_1 > T_2 > T_3 > T_4$).

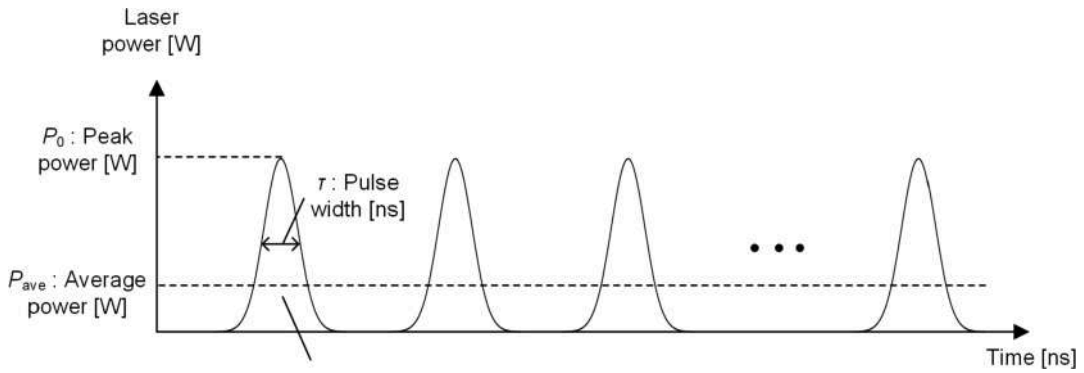

Fig. 3. Gaussian pulse train of laser irradiations.

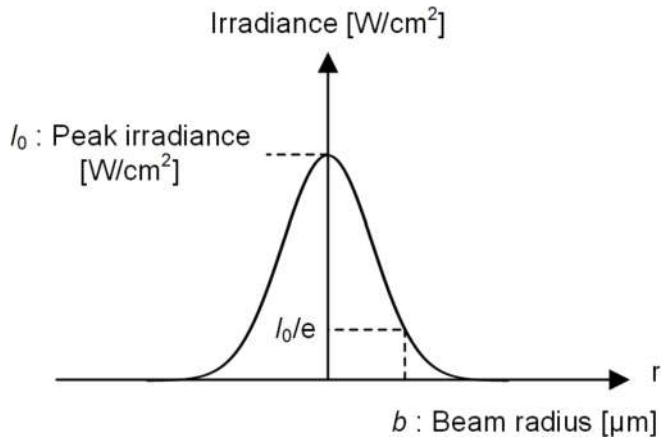

Fig. 4. Beam profile diagram with a Gaussian distribution.

26, and 38 ns were chosen for laser irradiation at a repetition frequency of 60, 100, and 150 kHz, respectively. To keep pulses overlap, the laser scanning speed was set to 51.0, 85.0, and 127.5 mm/s, according to repetition frequencies 60, 100, and 150 kHz at a scan pitch of 13.3 μm. In order to evaluate the effect of pulse width, not only laser fluence but also peak irradiance was used as parameters. The laser irradiation conditions are summarized in Table 1.

After laser irradiation, the surface topography of samples was measured by using a white-light interferometer Talysurf CCI 1000 (AMETEK Taylor Hobson Ltd., UK), a scanning electron microscope (SEM) Inspect S50 (FEI Company, USA), and an atomic force microscope (AFM) AFM5100 N (Hitachi High-Technologies Co., Japan). Crystallinity of the sample was analyzed by a laser micro-Raman spectrometer NRS-3100 (JASCO Co., Japan). The laser wavelength of the Raman spectrometer was 532 nm and the beam diameter was 1 μm.

In order to observe the subsurface damages of the grinded wafer,

Table 1
Laser irradiation conditions.

Pulse width (ns)	16	26	38
Repetition frequency (kHz)	60	100	150
Average power (W)	0.90–5.40	1.50–9.00	2.25–13.50
Laser fluence (J/cm^2)	0.26–1.59		
Peak irradiance ($\times 10^7$ W/cm^2)	8.81–52.84	5.42–32.52	1.31–7.84
Scanning speed (mm/s)	51.0	85.0	127.5

KOH solution etching was carried out. The concentration of the KOH solution was 1.0 mol/L (5.4%) and the temperature of the solution was kept 60 °C with a heater. The sample was fixed on a jig vertically and a half of the sample was immersed into the KOH solution. In this way, a step was obtained at the boundary of KOH solution surface, from which the etching depth was measured. The measured etching depth mainly results from the grinding-induced amorphous layer and the dislocated/cracked crystalline layer beneath the amorphous layer. The etching rate of the undamaged single-crystal bulk is distinctly lower, thus its contribution to etching depth can be neglected. The etching time was set to 200 s. Depth of etching was measured by using a laser probe profilometer MP-3 (Mitaka Kohki Co., Ltd., Japan).

4. Results and discussion

4.1. Effect of pulse width and peak irradiance

Fig. 5 shows three-dimensional surface topographies at different laser peak irradiances with a pulse width of 36 ns The topography of the original surface before laser irradiation is shown in Fig. 5(a). There were grinding marks on the surface. When the laser peak irradiance was 1.31 $\times 10^7$ W/cm^2, the surface was slightly rougher than the original surface (Fig. 5(b)). As shown in Fig. 5(c), grinding marks were smoothed by laser irradiation at a laser peak irradiance of 2.61 $\times 10^7$ W/cm^2, while surface waviness still remained. Under this condition, the melted silicon

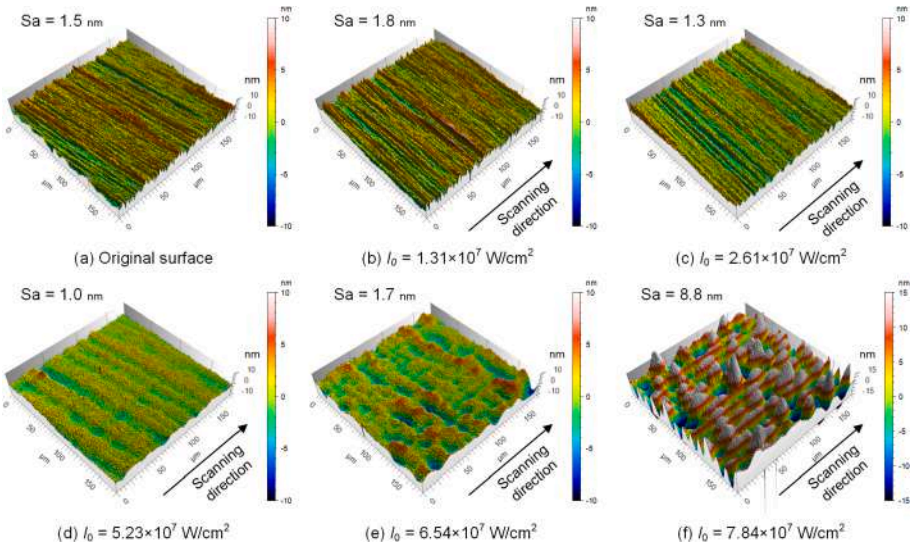

Fig. 5. Three-dimensional surface topographies at different laser peak irradiances with a pulse width of 36 ns; (a) original surface, (b) 1.31 × 10^7 W/cm^2, (c) 2.61 × 10^7 W/cm^2, (d) 5.23 × 10^7 W/cm^2, (e) 6.54 × 10^7 W/cm^2, and (f) 7.84 × 10^7 W/cm^2.

layer was extremely thin, thus the surface tension effect was insufficient to flatten the waviness. As laser peak irradiance increased to 5.23 × 10^7 W/cm^2, the surface became flat (Fig. 5(d)). In this case, the thickness of melted silicon layer was large enough to enhance the surface tension effect. When the laser peak irradiance increased to 6.54 × 10^7 W/cm^2, the surface became rough again (Fig. 5(e)). When the laser peak irradiance reached 7.84 × 10^7 W/cm^2, parallel grooves were observed on the surface as shown in Fig. 5(f), which were produced by the laser scan.

Even though the same laser fluence was used, the surface roughness changed with pulse widths. Fig. 6 shows a replot of surface roughness versus laser peak irradiance and pulse widths. In case of 38 ns pulse width, the surface roughness at peak irradiance of 1.31 × 10^7 W/cm^2 was worse than that of original surface. Generally, microcracks are generated under the amorphous layer in grinding. It is difficult to measure the internal microcracks from the surface. During laser irradiation at a low peak irradiation, thermal expansion made the internal microcracks open rather than melting the material layer. The open cracks are measurable, leading to an increased surface roughness. By increasing laser peak irradiance to induce melting, the surface roughness decreased. The microcracks completely disappeared at a higher peak

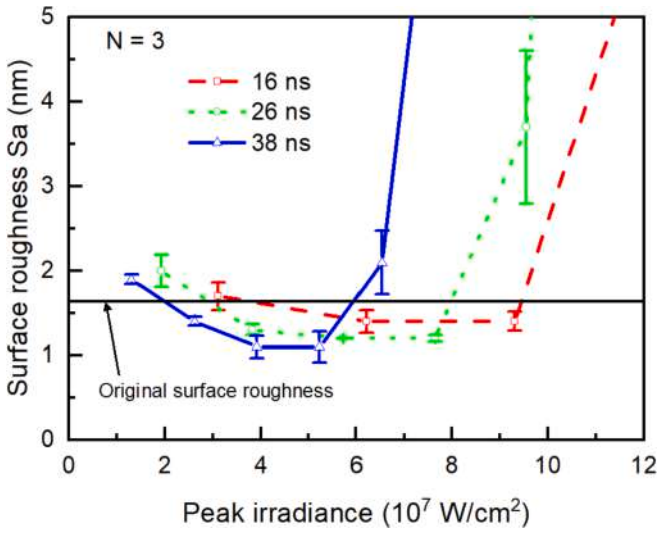

Fig. 6. Surface roughness of the irradiated silicon wafers at various laser peak irradiances and pulse widths.

irradiance which could melt and recrystallize the material deeply. However, when the laser peak irradiance is over 7.84 × 10^7 W/cm^2, the surface roughness increased sharply again. Under this condition, the parallel grooves roughened the surface. By decreasing pulse width, the surface roughness graph shifted to the right. Furthermore, the surface roughness was reduced by using a longer pulse width. The minimum surface roughness, Sa = 1.1 nm, was found at a peak irradiance ranging from 3.92 × 10^7 to 5.23 × 10^7 W/cm^2 at a pulse width of 38 ns

Fig. 7 shows SEM images of silicon wafer surfaces before laser irradiation and after laser irradiation with different laser peak irradiance at a pulse width of 38 ns As shown in Fig. 7(a), grinding-induced scratches and debris were observed on the original surface. At a low peak irradiance of 1.31 × 10^7 W/cm^2 (Fig. 7(b)), scratches remained and there is no significant change from the original surface. As the peak irradiance increases to 2.61 × 10^7 W/cm^2 (Fig. 7(c)), grinding-induced scratches disappeared and nanodot structures were observed. By increasing peak irradiance to 6.54 × 10^7 W/cm^2, not only nanodot structures but also ripple lines structures, which were clearly different from grinding-induced scratches, were generated, as shown in Fig. 7(e). The period of the ripples was approximately 532 nm which was the same as the laser wavelength. This ripple is called low-spatial-frequency LIPSS (LSFL) generated by surface electromagnetic wave which includes surface plasmon polaritons. Although the circular polarization was used for irradiation, LSFL was observed. By using a further higher laser peak irradiance of 7.84 × 10^7 W/cm^2, longer ripple line structures formed (Fig. 7(f)). Particle generation was also observed. These particles would be scattered by laser irradiation and reattached to the surface during recrystallizing process [9]. Thus, evaporation of material occurred during laser irradiation.

In order to measure the surface topography in detail, the original surface and laser irradiated surface at a peak irradiance of 5.23 × 10^7 W/cm^2 and pulse width of 38 ns were scanned by AFM as shown in Fig. 8. The surface profiles measured along lines 1–3 in Fig. 8(a) and (b) are shown in Fig. 8 (c)–(e), respectively. The arrows denote the directions of measurement. The height of grinding-induced ridges decreased from 30 to 50 nm–~10 nm by laser irradiation as shown in Fig. 8(c) and (d). The width of a nanodot was approximately 150 nm and the height was about 8 nm.

4.2. Effect of laser scan repetition

Fig. 9 shows SEM images of laser irradiated silicon surfaces at a pulse

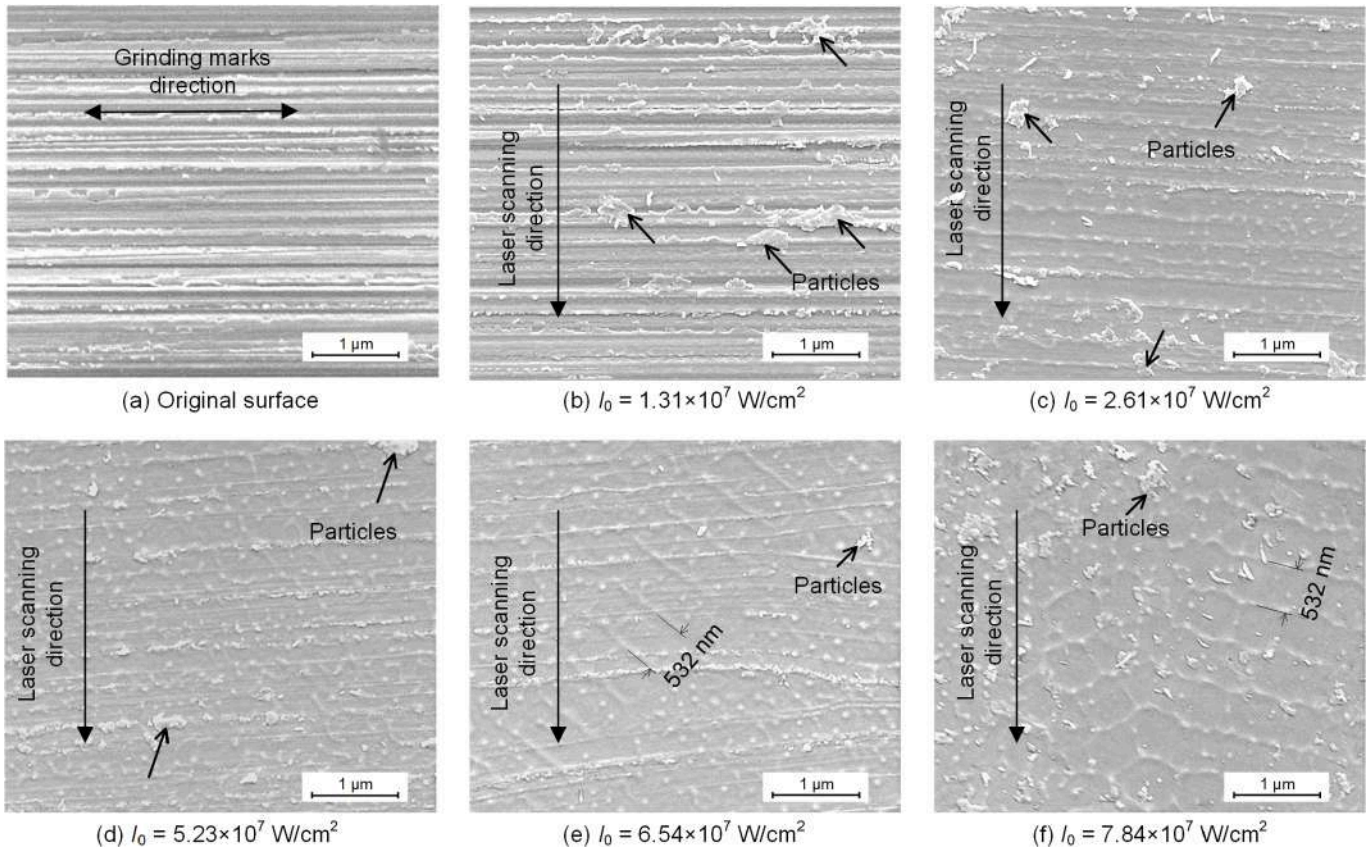

Fig. 7. SEM images of silicon wafer samples: (a) original surface by grinding; laser-irradiated surface at (b) 1.31 × 10^7 W/cm^2, (c) 2.61 × 10^7 W/cm^2, (d) 5.23 × 10^7 W/cm^2, (e) 6.54 × 10^7 W/cm^2, and (f) 7.84 × 10^7 W/cm^2.

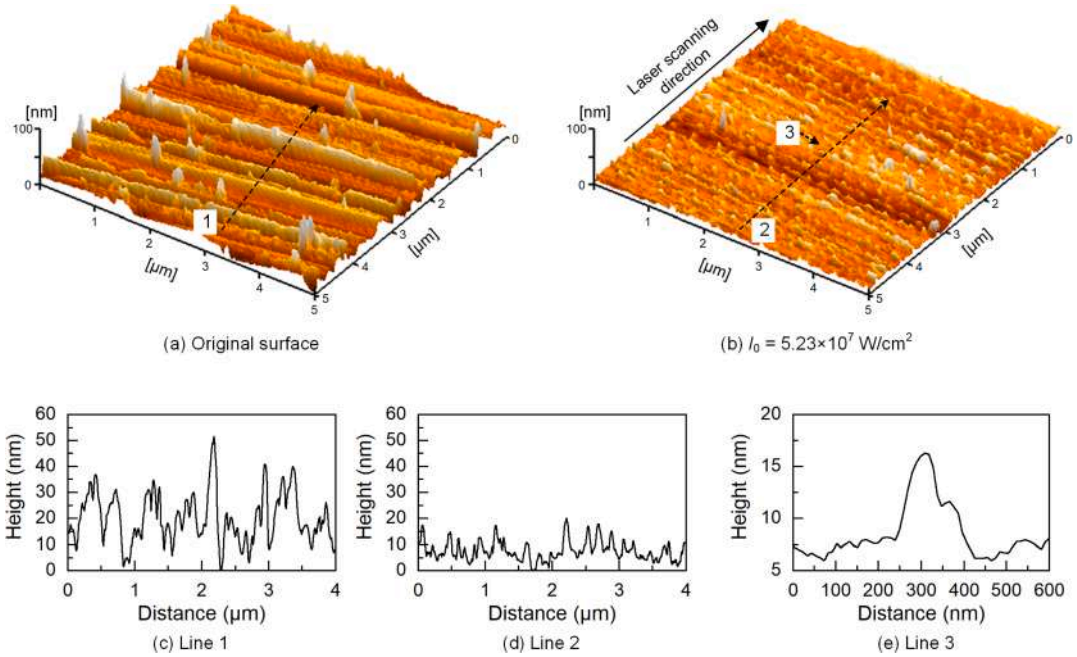

Fig. 8. AFM images of silicon wafer surfaces: (a) before laser irradiation; (b) after laser irradiation at peak irradiance of 5.23 × 10^7 W/cm^2 and pulse width of 38 ns; (c)–(e): surface profiles measured along lines 1–3 in (a) and (b).

width of 38 ns and a laser peak irradiance of 5.23 × 10^7 W/cm^2 with different number of laser scanning repetitions. As shown in Fig. 9(a), grinding marks vanished in laser-affected region. The surface became flat after laser irradiation. By increasing the number of scan repetitions, crisscross lines in different directions from the grinding marks appeared. The crisscross lines became more apparent when the scan number increased. High-magnification SEM micrographs of the laser irradiated surfaces are shown in Fig. 10. As the number of laser scan repetition

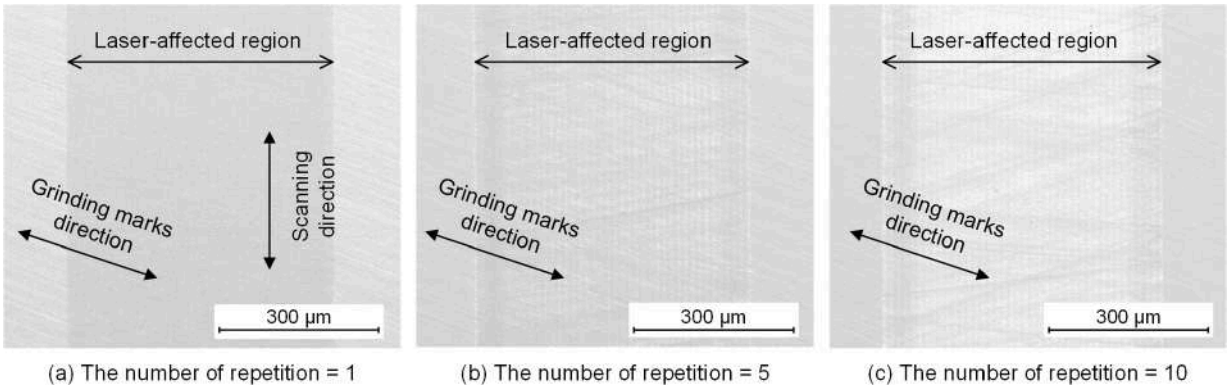

Fig. 9. SEM images of laser irradiated surface at a pulse width of 38 ns and a laser peak irradiance of 5.23×10^7 W/cm^2 with different number of repetitions: (a) 1, (b) 5, and (c) 10.

increased, the number and the size of nanodots increased. Region A indicated in Fig. 10(c) correspond to a part of a crisscross line. It was observed that the nanodots in region A were larger than those in other areas, and were integrated with each other.

In order to measure the height of nanodots, AFM mapping was performed. As shown in Fig. 11(a), nanodots with various sizes existed on the surface. While the height of the smaller nanodots was less than 10 nm, that of larger ones were approximately 50 nm. When the number of scan repetitions increased, the number and the height of big nanodots increased. As shown in Fig. 11 (c) and (f), many nanodots were aggregated to each other.

Fig. 12 shows normalized Raman spectra and full width at half maximum (FWHM) of the Raman peaks. The single-crystal silicon peak at 521 cm^{-1} [36] was observed for each spectrum while no obvious amorphous silicon peak at 470 cm^{-1} [36] was found. Normally, grinding produces an amorphous layer. However, the amorphous layer can be extremely thin (~a few nanometers) so that it is difficult to be detected by Raman spectroscopy [37]. In general, Raman peak shift shows residual stress [36,38–40] and FWHM shows crystallinity of a material [41–43]. At the original surface, the single-crystal silicon peak was shifted to 521.5 cm^{-1}, indicating residual compressive stress caused by grinding process [4,5]. After a single laser irradiation, the single-crystal silicon peak was returned to 521 cm^{-1}, the same as that of CMP. However, as increasing the number of scan repetitions to 10, the peak moved to a lower frequency, showing a tensile residual stress remained on the irradiated surface. The average FWHMs for ten measurements were compared in Fig. 12(b). It was confirmed that the FWHM of the grinded surface was wider than that of the CMP surface, indicating low crystallinity due to dislocations. After laser irradiation, however, the FWHM was improved to the same level as that of CMP.

Fig. 13 shows a micrograph of the laser irradiated surface indicated with a Raman mapping region. The surface was irradiated at a pulse width of 38 ns and a laser peak irradiance of 5.23×10^7 W/cm^2. Fig. 13 (b) shows Raman mapping images of peak intensity at the single-crystal silicon peak at 521 cm^{-1}. Fig. 13(c) shows the Raman mapping result of the FWHM of the single-crystal silicon peak. Although there were slight differences in peak intensity, the entire surface was single-crystal silicon. The crystallinity was almost uniform.

Fig. 14 shows the schematic diagrams of nanodots aggregation mechanism by multiple laser irradiations. After the first laser irradiation, a nanodot structure is generated as shown in Fig. 14(a). When the second laser irradiation is performed, the surface is melted (Fig. 14(b)), but the nanodot structures remain on the top of surface due to the combination of recoil pressure and surface tension effect. The recoil pressure keeps nanodot structure for 10 ns even there is surface tension in melting silicon [17]. Meanwhile, new protrusions are generated due to the Mullins-Sekerka instability during recrystallization (Fig. 14(c)). As a result of concurrence of previously generated nanodots and the newly generated ones, the nanodot structure increased on the top surface (Fig. 14(d)). As previously reported, smaller surface dots can be incorporated into larger ones due to Ostwald ripening [31,44]. If laser repetition increases, the number of nanodots increases and the probability of nanodots aggregation also increases. As a result, larger nanodot structures are created.

After laser recovery, the CMP process is required to remove the nanodot structures from the surface. However, the polishing allowance of nanodots is distinctly smaller than that of grinding-induced deep damages. Thus, the total wafer processing time will not increase dramatically due to the nanodots removal.

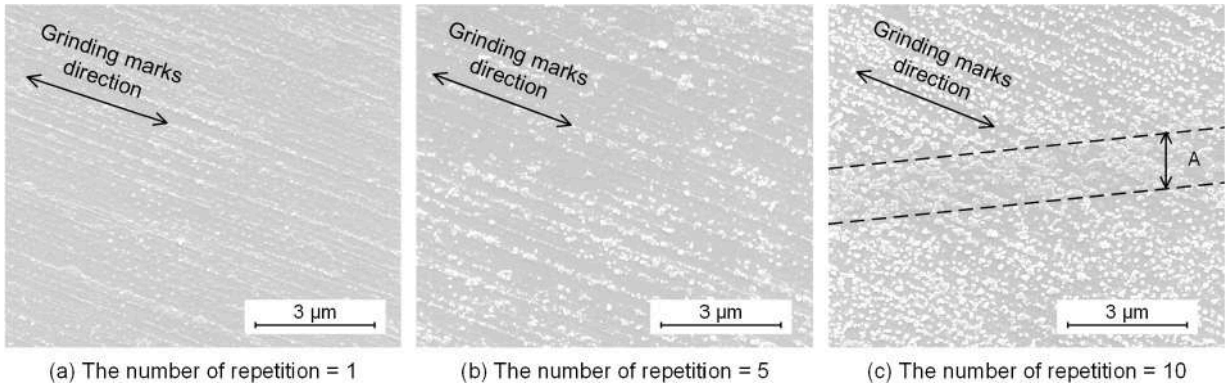

Fig. 10. High-magnification SEM images of the laser irradiated surfaces shwon in Fig. 9(a–c).

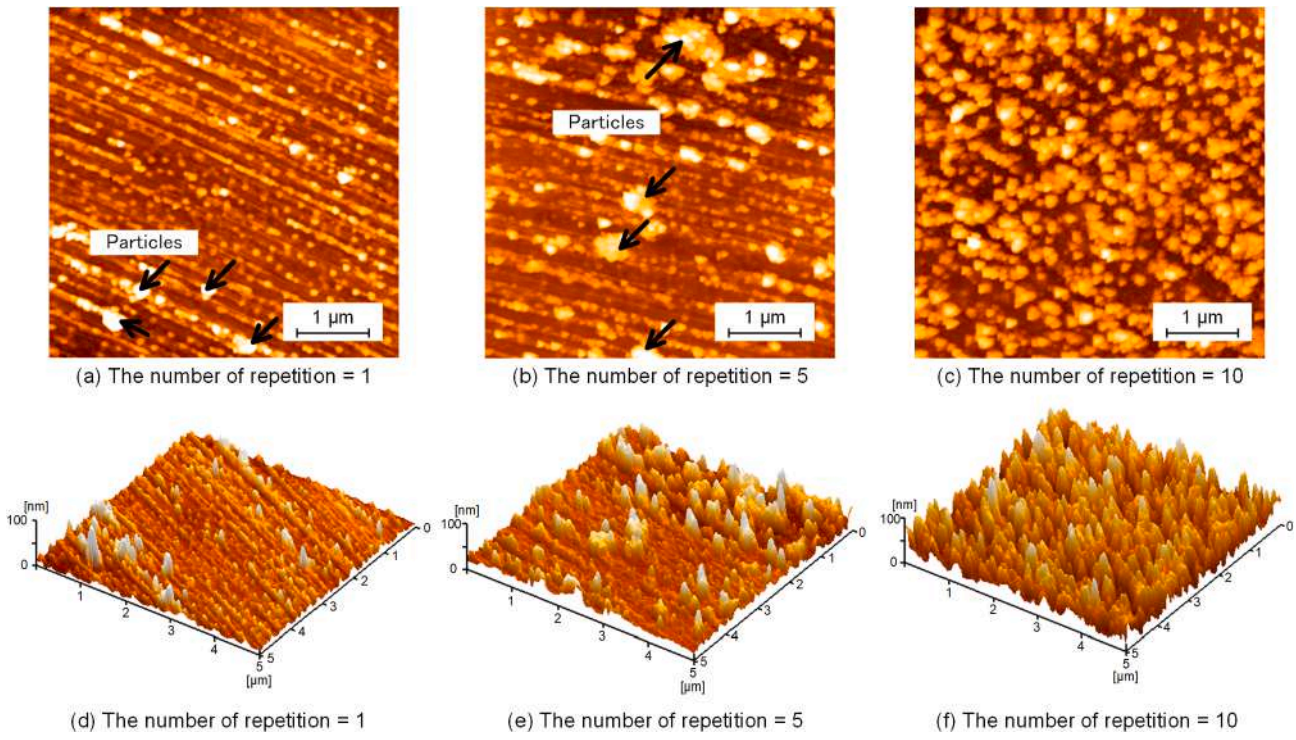

Fig. 11. AFM images of the laser irradiated surfaces shown in Fig. 10 (a–c).

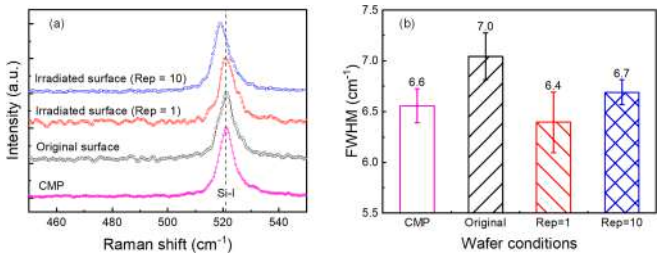

Fig. 12. (a) Normalized Raman spectra and (b) FWHM of spectra of CMP wafer, original surface, and laser-irradiated surface.

4.3. Effect of subsurface defects

One of the possible reasons for the crisscross lines in Fig. 9(c) might be the subsurface damages generated by the grinding process. Next, KOH etching was performed to investigate the cause of the crisscross line formation. Fig. 15 shows SEM images of silicon surface before and after KOH etching. After KOH etching, latent lines distinctly different from the grinding marks emerged on the surface. These latent lines were similar to the crisscross lines in Fig. 9(c). To measure the height difference between grinding marks and latent lines, the etched silicon wafer was measured by a white light interferometer. A two-dimensional surface topography of the etched surface is shown in Fig. 16. The latent lines were processed deeper than the grinding marks by KOH etching. As dislocations and amorphous layers have higher etching rates than single-crystal silicon, it is presumable that the grinding damages were not completely melted during laser irradiation, which affected the recrystallization. Therefore, the latent lines appeared after laser irradiation. It should be pointed out that the directions of the deep latent lines were completely different from that of the grinding marks on the top surface. The crisscross latent lines might have been generated in the previous rough grinding process, rather than the fine finish grinding. For flattening a wafer after wire sawing, simultaneous double-side grinding or single-side grinding by using cup wheels with coarse grain abrasives are performed [1]. These rough grinding processes generate crisscross grinding marks on the wafer surfaces [45,46]. In Fig. 16, the crisscross latent lines are presumably the deep subsurface damages caused by the rough grinding process before the fine grinding.

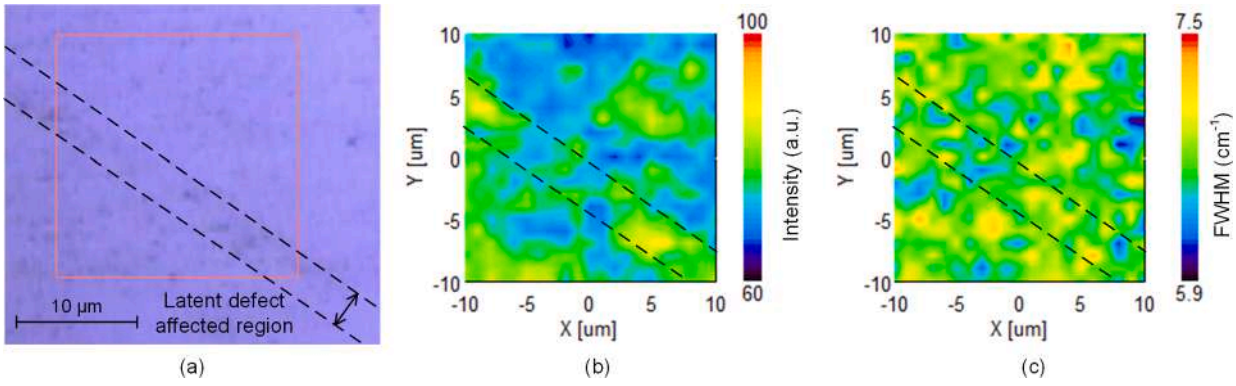

Fig. 13. (a) Surface micrograph indicated with a Raman mapping region; Raman mapping images of (b) peak intensity, and (c) FWHM at 521 cm^{-1}.

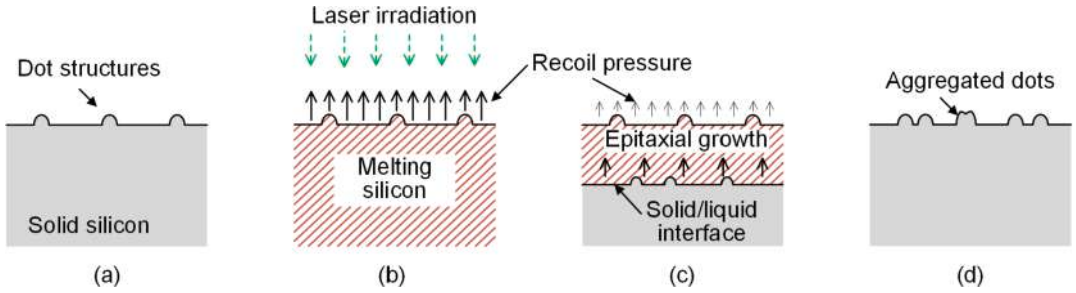

Fig. 14. Schematic diagrams of nanodots aggregation mechanism by laser irradiation.

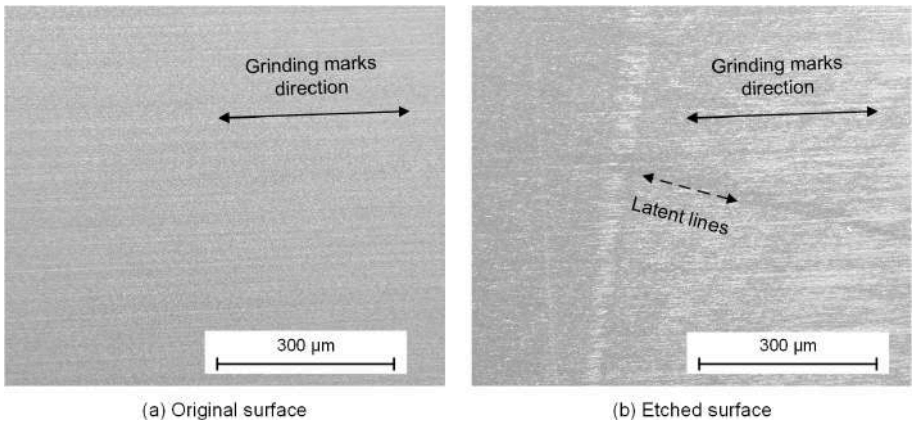

Fig. 15. SEM image of silicon surface before and after KOH etching.

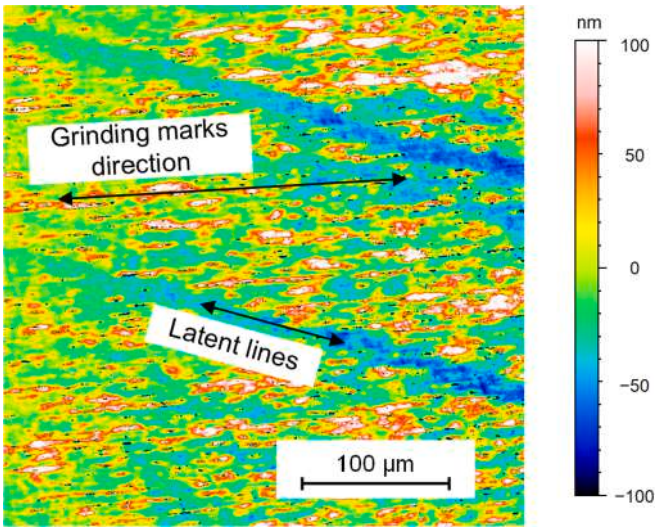

Fig. 16. Two-dimensional surface topography of silicon surface after KOH etching.

Fig. 17 shows a cross-sectional profile of the boundary between the original surface region and etched region. To eliminate noise in surface profiling, a low pass filter was used at a cut-off of $\lambda = 80$ μm. The average etched depth in three measurements was 459 ± 16 nm, which is roughly estimated as the subsurface damage depth.

To verify these results, laser irradiation at a higher peak irradiance was performed to melt a deeper layer. Fig. 18 shows SEM images of the laser irradiated surface at a pulse width of 38 ns and a laser peak irradiance of 6.54×10^7 W/cm^2. In this case, even when the number of laser scan repetitions was increased, the crisscross lines shown in Fig. 9 did not appear. The laser has melted a deep layer reaching the damage-free

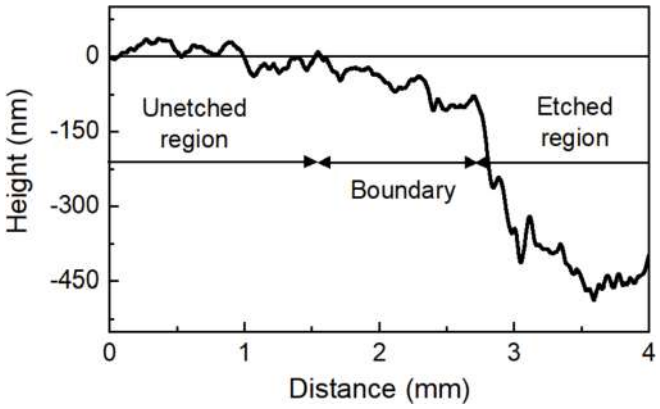

Fig. 17. Cross-sectional profile of the boundary between etched and unetched surface regions.

bulk, and all the damages could be recovered.

Based on the aforementioned results, the laser recovery mechanisms at different laser peak irradiances are proposed as follows. In the subsurface layer of a grinded wafer, latent damages such as dislocations and stacking fault generated in the rough grinding process are present although they cannot be seen from the top surface. During laser irradiation, when the laser peak irradiance is low, the melting layer does not reach the damage-free bulk. As a result, there will be a defected region grown from the latent damages after laser irradiation. This region causes interfacial instability, and surface protrusions is more likely to occur in this region than the bulk region. As a result, nanodots occur intensively on the top surface. On the other hand, when the laser peak irradiance is high, the latent damage layer is completely melted. The damage-free region acts as the seed for crystal regrowth. As a result, the nanodot structure on the top surface is reduced. The difference of nanodot

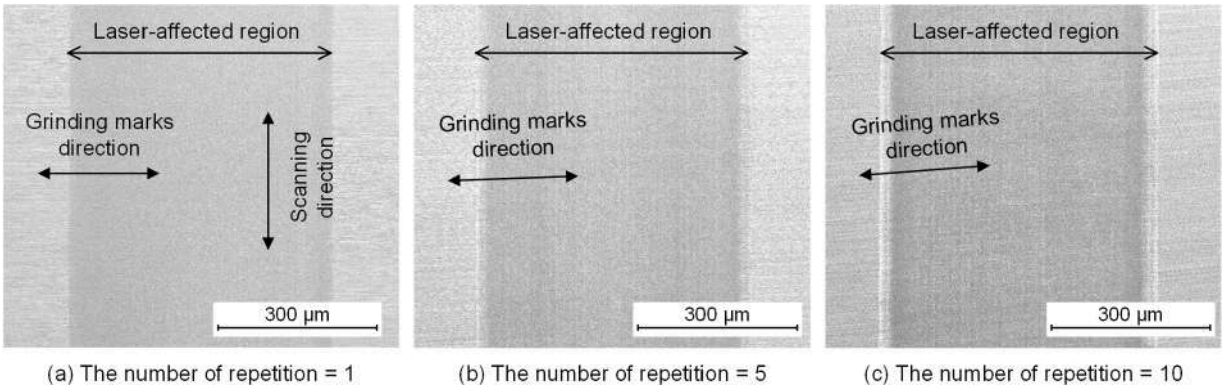

Fig. 18. SEM images of laser irradiated surface at a pulse width of 38 ns and a laser peak irradiance of 6.54×10^7 W/cm^2 with different number of repetition: (a) 1, (b) 5,and (c)10.

structure formation due to subsurface damages was acceptable evidence that Mullins-Sekerka instability generates protrusions.

It should be pointed out that in this study, the Raman spectra were detected from a thick surface layer due to that the penetration depth of a 532 nm-wavelength laser into single-crystal silicon is ~1 μm [37]. As a future task, the crystallinity of the surface layer up to a depth of tens of nanometers will be further evaluated in detail by higher resolution characterization methods to investigate its applicability to electronic devise fabrication.

5. Conclusions

A nanosecond pulsed Nd:YVO_4 laser was irradiated on a boron-doped single-crystal silicon wafer after rough and fine diamond grinding processes, and the surface nanostructure generation mechanism was investigated. The main findings include:

(1) The minimum surface roughness (1.1 nm Sa) was obtained at a peak irradiance ranging from 3.92×10^7 to 5.23×10^7 W/cm^2 and with a pulse width of 38 ns
(2) As the number of laser scan repetition increased, the number and size of nanodots increased, and a tensile residual stress was induced in the surface.
(3) Subsurface damages caused by rough grinding with cup wheels and coarse abrasive grains existed at a depth of ~459 nm. These subsurface damages affected nanodot structure formation on the surface and appeared on the surface as crisscross lines after multiple laser scan.
(4) Surface nanodot structures can be controlled by peak irradiance and pulse width.
(5) By using a sufficiently high laser peak irradiance (6.54×10^7 W/cm^2) and a suitable pulse width (38 ns), the laser melted layer reached the damage-free bulk. After the laser pulse, the entire subsurface damage layer could be recovered with insignificant surface nanodot generation.

The findings from this research will contribute to the laser processing of silicon wafers for reducing both deep subsurface damage and surface roughness. The laser recovery technology is especially useful as it can be applied to the finishing of curved surfaces such as wafer edges and notches, and other workpiece such as infrared lenses made of silicon.

Acknowledgment

The authors would like to extend thanks to Mr. Yu Tayama and Mr. Takatoshi Kato of SPEEDFAM Co., LTD for their help in silicon sample preparation. This work has been partially supported by Keio University KLL Research Grant for Ph.D. Program for 2019 Academic Year.

References

[1] Pei ZJ, Fisher GR, Liu J. Grinding of silicon wafers: a review from historical perspectives. Int J Mach Tool Manuf 2008;48:1297–307.
[2] Yan J, Asami T, Harada H, Kuriyagawa T. Fundamental investigation of subsurface damage in single crystalline silicon caused by diamond machining. Precis Eng 2009;33:378–86.
[3] Kovalchenko AM, Milman YV. On the cracks self-healing mechanism at ductile mode cutting of silicon. Tribol Int 2014;80:166–71.
[4] Zhou P, Yan Y, Huang N, Wang Z, Kang R, Guo D. Residual stress distribution in silicon wafers machined by rotational grinding. J Manuf Sci Eng 2017;139:081012.
[5] Zhou P, Xu S, Wang Z, Yan Y, Kang R, Guo D. A load identification method for the grinding damage induced stress (GDIS) distribution in silicon wafers. Int J Mach Tool Manuf 2016;107:1–7.
[6] Jingfei Y, Qian B, Yinnan L, Bi Z. Formation of subsurface cracks in silicon wafers by grinding. Nami Jishu Yu Jingmi Gongcheng/Nanotechnology Precis. Eng. 2018; 1:172–9.
[7] Yan J, Asami T, Harada H, Kuriyagawa T. Crystallographic effect on subsurface damage formation in silicon microcutting. CIRP Ann - Manuf Technol 2012;61: 131–4.
[8] Yan J, Asami T, Kuriyagawa T. Response of machining-damaged single-crystalline silicon wafers to nanosecond pulsed laser irradiation. Semicond Sci Technol 2007; 22:392–5.
[9] Yan J, Sakai S, Isogai H, Izunome K. Recovery of microstructure and surface topography of grinding-damaged silicon wafers by nanosecond-pulsed laser irradiation. Semicond Sci Technol 2009;24. 105018.
[10] Yan J, Kobayashi F. Laser recovery of machining damage under curved silicon surface. CIRP Ann - Manuf Technol 2013;62:199–202.
[11] Niitsu K, Tayama Y, Kato T, Maehara H, Yan J. Characterization of recrystallized depth and dopant distribution in laser recovery of grinding damage in single-crystal silicon. Mater Sci Semicond Process 2018;82:54–61.
[12] Niitsu K, Tayama Y, Kato T, Yan J. Laser recovery of grinding-induced subsurface damage in the edge and notch of a single-crystal silicon wafer. Surf. Topogr. Metrol. Prop. 2019;7:015013.
[13] Bonse J, Krüger J. Pulse number dependence of laser-induced periodic surface structures for femtosecond laser irradiation of silicon. J Appl Phys 2010;108.
[14] Gnilitskyi I, Gruzdev V, Bulgakova NM, Mocek T, Orazi L. Mechanisms of high-regularity periodic structuring of silicon surface by sub-MHz repetition rate ultrashort laser pulses. Appl Phys Lett 2016;109.
[15] Ji X, Jiang L, Li X, Han W, Liu Y, Wang A, Lu Y. Femtosecond laser-induced cross-periodic structures on a crystalline silicon surface under low pulse number irradiation. Appl Surf Sci 2015;326:216–21.
[16] Le Harzic R, Stracke F, Zimmermann H. Formation mechanism of femtosecond laser-induced high spatial frequency ripples on semiconductors at low fluence and high repetition rate. J Appl Phys 2013;113.
[17] Tsibidis GD, Barberoglou M, Loukakos PA, Stratakis E, Fotakis C. Dynamics of ripple formation on silicon surfaces by ultrashort laser pulses in subablation conditions. Phys Rev B - Condens Matter Mater Phys 2012;86:1–14.
[18] Tsibidis GD, Fotakis C, Stratakis E. From ripples to spikes: a hydrodynamical mechanism to interpret femtosecond laser-induced self-assembled structures. Phys Rev B - Condens Matter Mater Phys 2015;92:1–6.
[19] Miyaji G, Hagiya M, Miyazaki K. Excitation of surface plasmon polaritons on silicon with an intense femtosecond laser pulse. Phys. Rev. B 2017;96:1–6.
[20] Sub–damage–threshold femtosecond laser ablation from crystalline Si: surface nanostructures and phase transformation. Appl. Phys. 2004;79:1429–32.
[21] Varlamova O, Costache F, Reif J, Bestehorn M. Self-organized pattern formation upon femtosecond laser ablation by circularly polarized light. Appl Surf Sci 2006; 252:4702–6.
[22] Varlamova O, Reif J, Varlamov S, Bestehorn M. The laser polarization as control parameter in the formation of laser-induced periodic surface structures: comparison of numerical and experimental results. Appl Surf Sci 2011;257:5465–9.

[23] Trtica MS, Gakovic BM, Radak BB, Batani D, Desai T, Bussoli M. Periodic surface structures on crystalline silicon created by 532 nm picosecond Nd:YAG laser pulses. Appl Surf Sci 2007;254:1377–81.
[24] Talbi A, Kaya-Boussougou S, Sauldubois A, Stolz A, Boulmer-Leborgne C, Semmar N. Laser-induced periodic surface structures formation on mesoporous silicon from nanoparticles produced by picosecond and femtosecond laser shots. Appl Phys A Mater Sci Process 2017;123:1–7.
[25] Sarbada S, Huang Z, Shin YC, Ruan X. Low-reflectance laser-induced surface nanostructures created with a picosecond laser. Appl Phys A Mater Sci Process 2016;122:1–10.
[26] Mezera M, Römer GRBE. Model based optimization of process parameters to produce large homogeneous areas of laser-induced periodic surface structures. Opt Express 2019;27:6012.
[27] Hongo M, Matsuo S. Subnanosecond-laser-induced periodic surface structures on prescratched silicon substrate. Appl. Phys. Express. 2016;9:7–10.
[28] Yoshida Y, Sakaguchi N, Watanabe S, Kato T. Self-organized two-dimensional vidro-nanodot array on laser-irradiated Si surface. Appl. Phys. Express. 2011;4.
[29] Yoshida Y, Oosawa K, Wajima J, Watanabe S, Matsuo Y, Kato T. Nanosecond pulsed laser induced self-organized nano-dots patterns on GaSb surface. Appl Surf Sci 2014;307:24–7.
[30] Weizman M, Nickel NH, Sieber I, Yan B. Laser-induced self-organization in silicon-germanium thin films. J Appl Phys 2008;103.
[31] Watanabe S, Yoshida Y, Kayashima S, Yatsu S, Kawai M, Kato T. In situ observation of self-organizing nanodot formation under nanosecond-pulsed laser irradiation on Si surface. J Appl Phys 2010;108.
[32] Nürnberger P, Reinhardt HM, Kim HC, Pfeifer E, Kroll M, Müller S, Yang F, Hampp NA. Orthogonally superimposed laser-induced periodic surface structures (LIPSS) upon nanosecond laser pulse irradiation of SiO 2/Si layered systems. Appl Surf Sci 2017;425:682–8.
[33] Nayak BK, Sun K, Rothenbach C, Gupta MC. Self-organized 2D periodic arrays of nanostructures in silicon by nanosecond laser irradiation. Appl Opt 2011;50:2349.
[34] Hatano M, Moon S, Lee M, Suzuki K, Grigoropoulos CP. Excimer laser-induced temperature field in melting and resolidification of silicon thin films. J Appl Phys 2000;87:36–43.
[35] Mullins WW, Sekerka RF. Morphological stability of a particle growing by diffusion or heat flow. J Appl Phys 1963;34:323–9.
[36] Gogotsi Y, Baek C, Kirscht F. Raman microspectroscopy study of processing-induced phase transformations and residual stress in silicon. Semicond Sci Technol 1999;14:936–44.
[37] Yan J, Asami T, Kuriyagawa T. Nondestructive measurement of machining-induced amorphous layers in single-crystal silicon by laser micro-Raman spectroscopy. Precis Eng 2008;32:186–95.
[38] Lucazeau G, Abello L. Micro-Raman analysis of residual stresses and phase transformations in crystalline silicon under microindentation. J Mater Res 1997; 12:2262–73.
[39] Sparks RG, Paesler MA. Micro-Raman analysis of stress in machined silicon and germanium. Precis Eng 1988;10:191–8.
[40] Paillard V, Puech P, Laguna Ma, Temple-Boyer P, Caussat B, Couderc JP, De Mauduit B. Resonant Raman scattering in polycrystalline silicon thin films. Appl Phys Lett 1998;73:1718–20.
[41] Ogura A, Kakemura Y, Kosemura D, Yoshida T, Masaki M, Nishida K, Kawakami R, Yamamoto N. Evaluation of poly-Si thin film crystallized by solid green laser annealing using UV/visible Raman spectroscopy. J Mater Sci Mater Electron 2008; 19:122–6.
[42] Xu Z, He Z, Song Y, Fu X, Rommel M, Luo X, Hartmaier A, Zhang J, Fang F. Topic review: application of Raman spectroscopy characterization in micro/nano-machining. Micromachines 2018;9:361.
[43] Arnaud Z, editor. Raman imaging. Springer-Verlag Berlin Heidelberg; 2012.
[44] Ross FM, Tersoff J, Tromp RM. Ostwald ripening of self-assembled germanium Islands on silicon(100). Microsc Microanal 1998;4:254–63.
[45] Pietsch GJ, Kerstan M. Understanding simultaneous double-disk grinding: operation principle and material removal kinematics in silicon wafer planarization. Precis Eng 2005;29:189–96.
[46] Li Z, Lin B, Sun W, Zhang X. Simultaneous double side grinding of silicon wafers: a further investigation into grinding marks. Pattern 2010;27:395–400.